

# Infrared thermography for detection of laminar–turbulent transition in low-speed wind tunnel testing

Liselle A. Joseph<sup>1</sup> · Aurelien Borgoltz<sup>1</sup> · William Devenport<sup>1</sup>

Received: 22 September 2015 / Revised: 5 April 2016 / Accepted: 9 April 2016 / Published online: 30 April 2016  
© Springer-Verlag Berlin Heidelberg 2016

**Abstract** This work presents the details of a system for experimentally identifying laminar-to-turbulent transition using infrared thermography applied to large, metal models in low-speed wind tunnel tests. Key elements of the transition detection system include infrared cameras with sensitivity in the 7.5- to 14.0- $\mu\text{m}$  spectral range and a thin, insulating coat for the model. The fidelity of the system was validated through experiments on two wind-turbine blade airfoil sections tested at Reynolds numbers between  $Re = 1.5 \times 10^6$  and  $3 \times 10^6$ . Results compare well with measurements from surface pressure distributions and stethoscope observations. However, the infrared-based system provides data over a much broader range of conditions and locations on the model. This paper chronicles the design, implementation and validation of the infrared transition detection system, a subject which has not been widely detailed in the literature to date.

## 1 Introduction

Infrared thermography (IRT) is a boundary layer transition sensing method that depends on differences in model surface temperature caused by variations in the surface heat transfer rate associated with laminar and turbulent boundary layers. It is a nonintrusive method that does not suffer some of the drawbacks of competing methods. Unlike pointwise methods such as stethoscopes (Maughmer and Coder 2010; Mueller 2001), surface hot films (Tropea

et al. 2007) and pressure distribution analysis (Popov et al. 2008), IRT provides a global view of the transition front. Unlike surface oil-flow visualization and naphthalene visualization (Dagenhart et al. 1989; Radzetsky et al. 1994), the IRT technique offers the potential for consecutive measurement of multiple test points in a single tunnel run. Unlike temperature- and pressure-sensitive paints (Tropea et al. 2007), IRT does not require model painting and, in some cases, may need no special surface preparation at all.

Details of the method by which infrared thermography for transition detection can be applied in low-speed wind tunnel testing have not been widely reported. This method is usually attempted in hypersonic (Le Sant et al. 2002), supersonic (Zuccher and Saric 2008) and transonic (Le Sant et al. 2002) flows because of the inherently higher heat transfer rates which exist in high-speed flows. Moreover, most of the low-speed infrared systems reported to date (Ricci and Sergio Montelpare 2009; Yokokawa 2005; Quast 1987) have only focused on small-scale testing of single models at few angles of attack.

One of the primary goals (and complications) of the low-speed studies has been to develop a method for creating and maintaining a temperature difference between the model and the flow to augment the difference in heat transfer between the laminar and turbulent regions. Techniques which have been investigated include pre-treating the model [e.g., with cooling blankets (Yokokawa 2005) or liquid nitrogen (Zuccher and Saric 2008)] or using continuous mechanisms such as electrical elements in the model wall (Zuccher and Saric 2008; Ricci and Sergio Montelpare 2009; De Luca et al. 1990; Paturski et al. 2000; De Luca et al. 1995), internal heating sheets (Crawford et al. 2014), and heat lamps (Baek and Fuglsang 2009; Freels 2012; Gaidos 1990). While proven to work, the pre-treatment methods are inefficient for large-scale wind tunnel

✉ William Devenport  
devenport@vt.edu

<sup>1</sup> Department of Aerospace and Ocean Engineering, Virginia Tech, 215 Randolph Hall, Blacksburg, VA 24061, USA

tests because the temperature difference cannot be re-introduced as necessary during the test as is possible with the active methods. Consequently, when testing on large scales where runs can last for over an hour, an active method is more appropriate to create and maintain the temperature difference.

The use of infrared thermography with aluminum models has also been debated in past research. Due to the high thermal conductivity of metal models, some studies (Zuccher and Saric 2008; Freels 2012) suggest that these are not good candidates for testing using infrared thermography. Aluminum and most metals also reflect infrared radiation, which leads to obscured images (Zuccher and Saric 2008; Ehrmann and White 2014; Gompertz et al. 2012). The most successful model candidates for infrared thermography have low thermal conductivity, such as fiberglass and large emissivity. Nonetheless, the high conductivity properties of aluminum make the heating and cooling process efficient and easy, a characteristic that can be useful in commercial tests. Aluminum is also a popular material used in model fabrication.

This paper describes the development and implementation of an innovative infrared thermography system which efficiently detects transition on large (1.82-m) span, aluminum models at low speeds, producing clear images of the transition front. The results produced were validated by mean pressure and stethoscope measurements. A comprehensive account of this work is detailed in Joseph (2014) and summarized in Joseph et al. (2014).

## 2 Apparatus and instrumentation

### 2.1 Stability wind tunnel

Tests were conducted in the Virginia Tech Stability Wind Tunnel. This is a closed-circuit, continuous, single-return subsonic facility. For the current study, the Stability Wind Tunnel was run with the aerodynamic, hard wall test section shown in Fig. 1. This test section has a 1.83-m square cross section and is 7.3 m long. A turntable and support shafts are used to vertically mount 1.82-m span airfoils at the test section center (3.56 m from its upstream end) and rotate them to angle of attack about the quarter chord point. The flow in the empty test section has turbulence levels as low as 0.016 % at  $12 \text{ ms}^{-1}$  increasing with speed to 0.031 % at  $57 \text{ ms}^{-1}$  (Joseph 2014).

The wind tunnel facility is equipped with four pressure measurement systems: static pressure taps embedded in the walls of the settling chamber and the 9:1 contraction nozzle, airfoil surface pressure taps, test section wall pressure taps and a traversing drag rake comprised of Pitot and static probes. Measurements from these systems are used

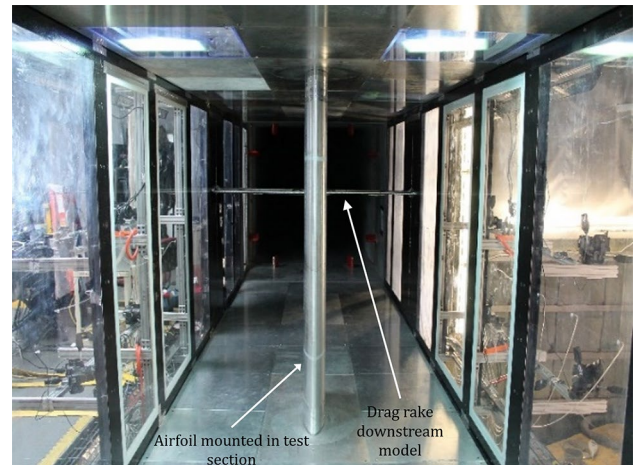


**Fig. 1** Upstream view of aerodynamic test section with 0.8-m DU96-W-180 and drag rake mounted inside

to estimate the flow speed and airfoil lift, pitching moment and drag. Blockage correction calculations are done according to the work of Allen and Vincenti (1947).

The facility also utilizes a boundary layer flow control system, which uses tip suction to ensure two-dimensional flow. This system extracts air from the tips of the model through 5-mm wide continuous slots around the perimeter of the airfoil. The suction system was used at all angles and all speeds during this series of tests in order to maintain maximum flow two-dimensionality.

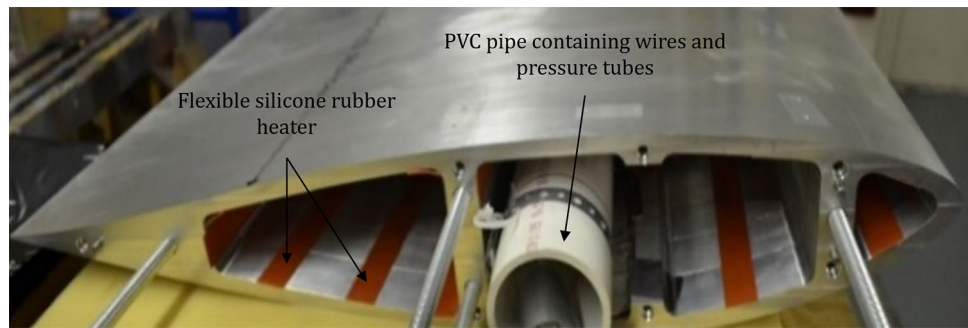
### 2.2 Airfoil models

0.8-m and a 0.46-m chord DU96-W-180 models were tested. Both were built from aluminum laminates stacked vertically to create a full 1.82-m span. Spanwise steps between laminates were typically 0.05 mm in height or less. Each of the laminates has internal open areas to allow instrumentation to be passed through the span of the model and for the center shaft to be inserted. The laminates have relatively small wall thickness compared to the chord length—average wall thicknesses are 13 mm for the 0.8-m chord model and 7 mm for the 0.46-m chord model. However, the leading and trailing edge regions of both models have larger material thicknesses as can be seen in Fig. 2. For pressure measurement, a total of 80 1-mm internal diameter pressure taps were drilled into the laminates of each model, around mid-span.

## 3 IRT transition detection system

The main requirement of the infrared thermography system was that it should be able to detect surface temperature

**Fig. 2** Cross section through 0.8-m DU96-W-180 with flexible silicone rubber heaters installed inside



differences of 2-K or less. This would ensure that the changes in temperature occurring as a result of laminar-to-turbulent transition could be accurately measured. Moreover, it was necessary that the system allows for the creation and maintenance of an adequate temperature difference between the model and the oncoming flow. This would ensure a versatile system by allowing the experimenter to choose a desired temperature difference at any point during the experiment. Additionally, all system components were required to be quick and easy to set up without permanent alteration to the model or significant modifications to any other measurement system.

### 3.1 Infrared camera and mounts

Two identical high-resolution, FLIR<sup>®</sup> A655sc infrared cameras were used for thermal imaging. This device has a spectral range between 7.5 and 14  $\mu\text{m}$  and an image resolution of  $640 \times 480$ . The noise equivalent temperature difference (NETD) is less than 30 mK for this camera. The FLIR<sup>®</sup> A655sc was calibrated by FLIR<sup>®</sup> Commercial Systems using NIST traceable equipment. This involved characterizing the camera detector response to a series of known temperature “blackbodies.” The reported accuracy of the camera is  $\pm 2\text{-K}$  or  $\pm 2\%$  of the reading, whichever is larger. Image acquisition was undertaken by use of the FLIR<sup>®</sup> Tools software.

Four circular holes of 63.5 mm diameter were cut in the walls of the test section, two per side, to mount the cameras. This was necessary to maximize the IR imaging quality as several materials (like regular glass or Lexan, from which the tunnel side walls are fabricated) filter IR radiations. It should be noted that during runs when infrared images were not being taken, circular rapid-prototyped pieces were inserted and secured into these holes to preserve the continuity of the test section walls. The camera mounting system was comprised of four pairs of Manfrotto<sup>®</sup> 808RC4 Quick Release tripod heads secured to a framework of 80/20<sup>®</sup> aluminum beams bolted to the outer flanges of the test section.

### 3.2 Airfoil modifications

In order to detect transition, it is crucial that there exists a temperature difference between the model and the oncoming flow. The work of Zuccher and Saric (2008), for example, compared three temperature states for infrared thermography on a Bakelite model: model at ambient temperature, heated model and a cooled model. The model at room temperature did not produce good results because the small temperature differences resulted in poor image resolution. Cooling the model with liquid nitrogen showed more promising results and better resolution than at room temperature. Finally, the model was heated by the use of electric elements connected to the model surface. Studies such as these gave several options for heating and cooling the model.

Preliminary tests revealed that an efficient and reliable means to create a temperature difference is to use lightweight, flexible, silicone rubber fiberglass insulated heaters (model SRFG-110/10-P) attached to the interior surfaces of the aluminum models. These heaters have a power density of  $15500 \text{ W/m}^2$  (total wattage of 100 W), an applied voltage of 110 V, and can withstand a maximum temperature of 422 K. Heaters were attached (by their pressure-sensitive adhesive backing) to the top 0.45 m of the span and mounted approximately 38.1 mm apart inside the model as shown in Fig. 2. The resulting power density on the model surface due to the action of the heaters has been estimated to be approximately  $450 \text{ W/m}^2$ .

In order to regulate the high rate of heat transfer from the aluminum models to the flow, an insulator was used on the model surface. This consisted of 0.8-mm-thick, black silicone rubber with an acrylic adhesive backing. This FDA compliant material was medium soft (durometer reading of 40A) and was purchased from McMaster-Carr (model number 8991K999). The insulator was applied to the model which was already covered in a layer of 88.9- $\mu\text{m}$ -thick black Contact<sup>®</sup> paper.

This model treatment was chosen based on the results of extensive preliminary tests which involved investigations

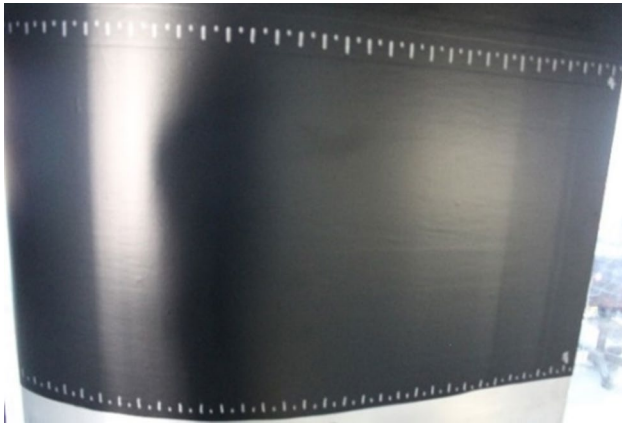


**Fig. 3** Suction side of the 0.8-m DU96-W-180 covered in 0.8-mm black silicone rubber insulator (leading edge on *left*)

into bare aluminum models (as was used by Yokokawa (2005) and Zuccher and Saric (2008) in short test runs) and aluminum models covered in insulating paints and other insulators [as was done by Freels (2012) and Ehrmann and White (2014)]. The insulators worked well in revealing transition, but the paints were time-consuming to apply and hard to remove, in most cases permanently altering the surface condition of the model. In addition, it was difficult to apply the paint uniformly and with equal thickness.

The issue of infrared reflections was circumvented in past research studies by increasing the model emissivity. Surface treatments which have been shown to work well include a thin layer of high emissivity, black paint as advocated by Zuccher and Saric (2008) and used by Ricci and Sergio Montelpare (2009), Schmitt and Chanetz (1985) and Le Sant et al. (2002). The surface emissivity of the models used in this study was increased by covering them with an additional sheet of 0.0889 mm (3.5 mils) thick, dull, black ConTact© paper. This covered the insulator which, despite being black, had a relatively low emissivity in the visible range of light due to its glossy finish. It should be noted here that since emissivity is a function of wavelength, the surface emissivity of the insulator in the infrared range will be different from that in the visible range. The final surface condition of the models was smooth, with no visible imperfections, as shown in Fig. 3.

The tick marks seen on the model surface in Fig. 3 were made using a silver Sharpie© because this metallic paint readily reflects infrared radiation making it visible on the infrared pictures. They are spaced every 12.7 mm, resulting in edge length values which can be converted to chord locations during image analysis. It should be noted that the 0.45-m section which contained the heaters and was covered by the insulator was located at approximately 0.15-m spanwise the pressure taps. This allowed both mean

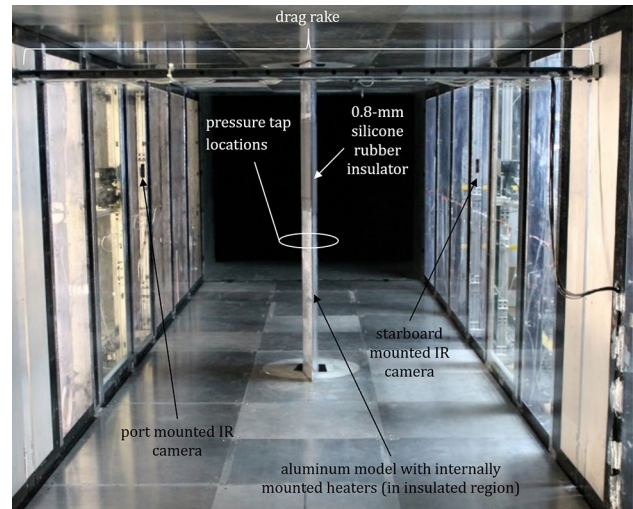


**Fig. 4** Downstream view of 0.46-m DU96-W-180 mounted in wind tunnel with infrared thermography system

surface pressure and infrared measurements to be taken simultaneously.

The complete infrared thermography system, with the 0.46-m chord DU96-W-180, is portrayed from downstream in Fig. 4. The setup for the 0.8-m DU96-W-180 was identical to that of the smaller chord model.

## 4 Alternative methods for transition detection

### 4.1 Mean pressure measurements

Surface pressure may be used as an indicator of transition. As laminar flow becomes turbulent, the increase in skin friction causes a measurable rise in the pressure and a peak in its second derivative (Popov et al. 2008). Practically, the accuracy of this technique is limited to the density of pressure taps on the airfoil, and the requirement that transition takes place at a streamwise location where other variations in the pressure distribution do not mask its signature, as is the case near the leading edge (Schmitt and Chanetz 1985). These limitations produce a 5 % chord uncertainty in the transition location results. Figure 5 shows an example of this method applied to the pressure coefficient distribution on the suction side of the 0.8-m DU96-W-180 at one condition.

### 4.2 Stethoscope observations

Transition was also detected using a stethoscope to listen for the rapid increase in surface pressure fluctuation levels associated with transition. An autocraft automotive stethoscope, (model AC637) attached to a Pitot probe, was used

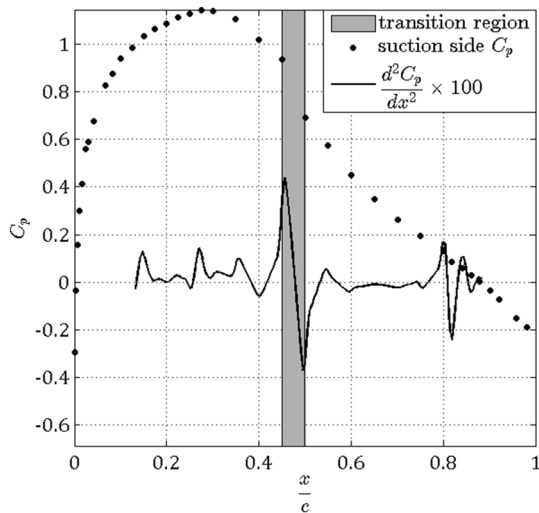
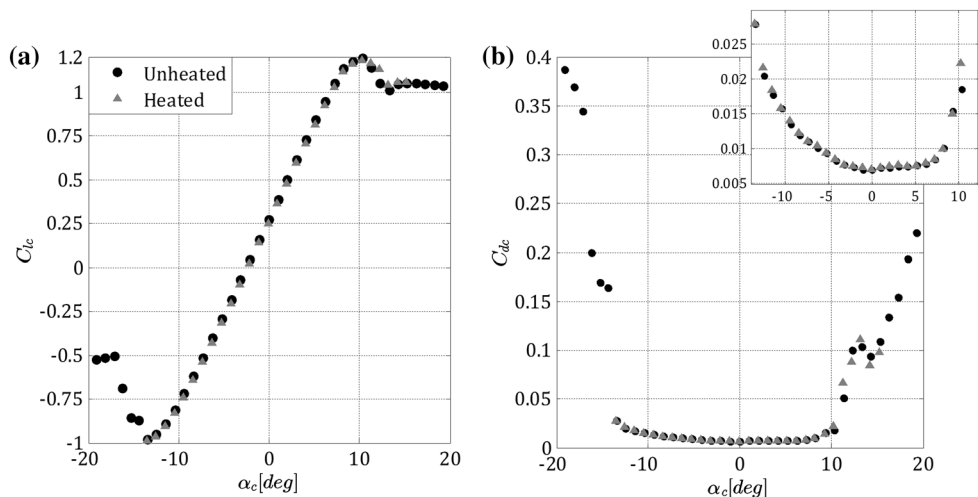


**Fig. 5** Measured surface pressure distribution and its second derivative on the suction side of the 0.8-m DU96-W-180 at  $Re = 1.5 \times 10^6$  and  $\alpha_c = 3^\circ$  showing the transition region between 45–50 % chord

for this test. The stethoscope diaphragm was replaced with thin Mylar sheet in order to improve the sensitivity. The Pitot probe was made of Precision Miniature 11 gauge stainless steel tubing (316 stainless steel) from McMaster-Carr (product number 89935K44). It has an outer diameter of 3.05 mm, inner diameter of 2.54 mm and a wall thickness of 0.25 mm. This tube was bent to approximately  $90^\circ$  to form the Pitot probe which would traverse the airfoil surface. A metal extension was made from hollow stainless steel and was 10 mm in diameter, 1.1 m long, to extend the Pitot probe into the test section. 1.8 mm diameter Tygon tubing was connected to the end of the Pitot probe and run through the length of the stainless steel extension to finally connect with the stethoscope.

**Fig. 6** Effects of heat on **a** coefficient of lift and **b** coefficient of drag at  $Re = 3 \times 10^6$  for the 0.8-m DU96-W-180



This device allowed the probe to be extended into the wind tunnel through the side walls so that experimenters could traverse the chord of the model, from leading to trailing edge, listening for increases in sound levels. The estimated uncertainty in detecting the sound changes using the stethoscope is  $\pm 13$ -mm along the edge of the model. For the 0.8-m model, this is  $\pm 3$  % chord and for the 0.46-m model this uncertainty translates to  $\pm 5.4$  % chord.

At most angles of attack, it was observed that there were two distinct sound changes over the airfoil chord, the second involving a greater increase in volume. These were attributed to the initiation and completion of transition, respectively. Consequently, the first sound change was taken as the transition location.

### 5 Preliminary assessment of the IRT transition detection system

Heating a model could change the behavior of the boundary layer and affect the overall flow on the model. Covering the model in a layer of any material adds some thickness to the profile which might also change the airfoil performance. The extents of these effects were investigated for the current system by examining them, independently and combined, the corrected lift,  $C_{l,c}$ , (obtained from integrating the wall pressure) and corrected drag,  $C_{d,c}$ , distributions for the 0.8-m DU96-W-180.

The effects of the rubber silicone insulator and heating the model proved to be negligible on their own, as detailed in Joseph (2014). This can be deduced from Fig. 6 which shows the individual effect of heating the 0.8-m chord DU96-W-180 by about 5-K at  $Re = 3 \times 10^6$ . All results are plotted with corrected angle of attack,  $\alpha_c$ . The good agreement observed between the heated and unheated lift

**Fig. 7** Combined effects of insulation and heat on **a** coefficient of lift  $Re = 3 \times 10^6$  and **b** coefficient of drag at  $Re = 3 \times 10^6$  for the 0.8-m DU96-W-180

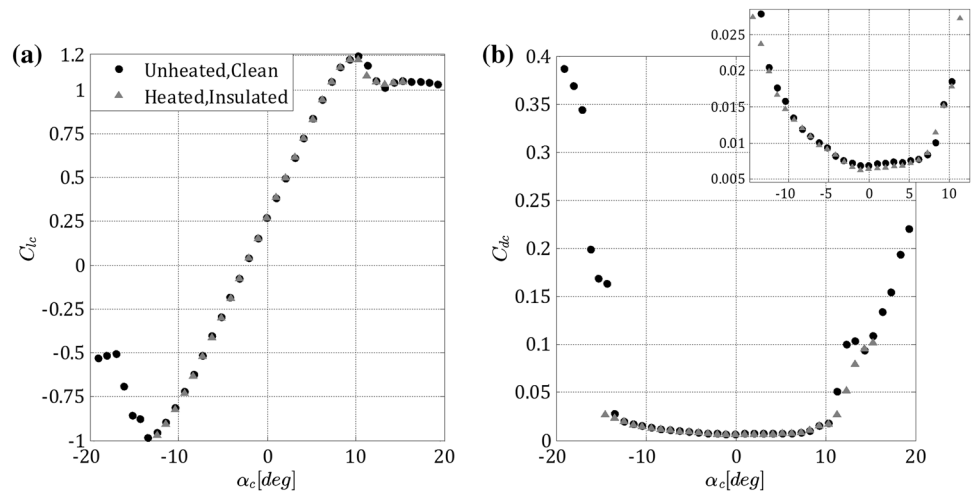


(Fig. 6a) and drag (Fig. 6b) curves suggests that heating the model does not have a significant effect on the flow. The combined effect of the insulator and heating the model was also found to be negligible by measuring the pressure over the chord of the heated (by about 5 to 6 K), insulated 0.8-m chord DU96-W-180. The corrected lift and corrected drag plots are shown in Fig. 7a, b for  $Re = 3 \times 10^6$ . All drag measurements were made at a spanwise location of 1117.6 mm above the floor. This location corresponds to 61.4 % of the insulated region (full span). Figures 6 and 7 show that the insulator and the heaters, when used individually and simultaneously, do not have a significant effect on the flow.

The lift curve for the heated/insulated model in Fig. 7a agrees well with the data from the clean airfoil, within an uncertainty of  $\pm 0.012$ . In the linear region, there is no indication of disagreement as both curves align well, having a slope of  $0.044 \text{ deg}^{-1}$ . Negative and positive stalls appears slightly delayed for the heated, insulated cases. This could simply be due to lack of repeatability in the stall behavior, but also could be due to the slight increase in thickness associated with the insulator covering. Similarly, the drag coefficient curves exhibit close agreement with each other with average error of 5 % except in the immediate vicinity of positive and negative stall. Differences here are likely due to three-dimensionality in the airfoil wake at stall, and thus sensitivity to the spanwise position of the drag rake. The results at  $Re = 1.5 \times 10^6$  and  $2 \times 10^6$  are not presented, but these also show good agreement between the clean, unheated model and the heated, insulated model.

In addition, an XFOIL study was done to investigate the effect of the insulator thickness on the model profile and showed that, at least for attached flow, the effects on lift and drag were less than 1 %. Supporting this, stethoscope measurements of the transition location on the clean and insulated model showed no significant differences within

the uncertainty of the measurements (see Joseph (2014) and Joseph et al. (2014) for detailed results).

## 6 IRT transition results

Measurements for the validation of the IRT system were made on the 0.8-m DU96-W-180 model at three Reynolds numbers:  $1.5 \times 10^6$ ,  $2 \times 10^6$  and  $3 \times 10^6$  and angles from  $-20^\circ$  to  $20^\circ$ , and on the 0.46-m model at two Reynolds numbers:  $1.5 \times 10^6$  and  $2 \times 10^6$  and angles from  $-20^\circ$  to  $20^\circ$ .

Figure 8 shows infrared images for both the pressure and suction sides of the 0.46-m model at  $Re = 1.5 \times 10^6$  and corrected angles of attack of  $\alpha_c = [0^\circ, -5^\circ, -7^\circ]$ . When viewing the pressure side of the model (Fig. 8a, c), the flow is observed from right to left, while the opposite is observed when viewing the suction side (Fig. 8b, d). In these images, the areas of lower temperature coincide with darker color while the regions of higher temperatures are whiter. Since the model is being heated, the large white regions represent the laminar flow and the darker regions turbulent flow. Hence, the transition can be identified as the region of highest chordwise temperature gradient—when the model surface becomes significantly cooler. In addition to the edge length markers on the model, there is also a vertical line drawn 228.6 mm (9 in.) from the trailing edge to be used by the image processing scheme. This line demarcates the forward, highly curved portion of the airfoil from the rearward, flatter region of the airfoil. This delineation is necessary so that the image processing algorithm can adequately account for the airfoil surface curvature between the leading and trailing edge when calculating the transition location.

Figure 8 also displays solid line plots of the temperature distribution along the chord of the model, extracted from

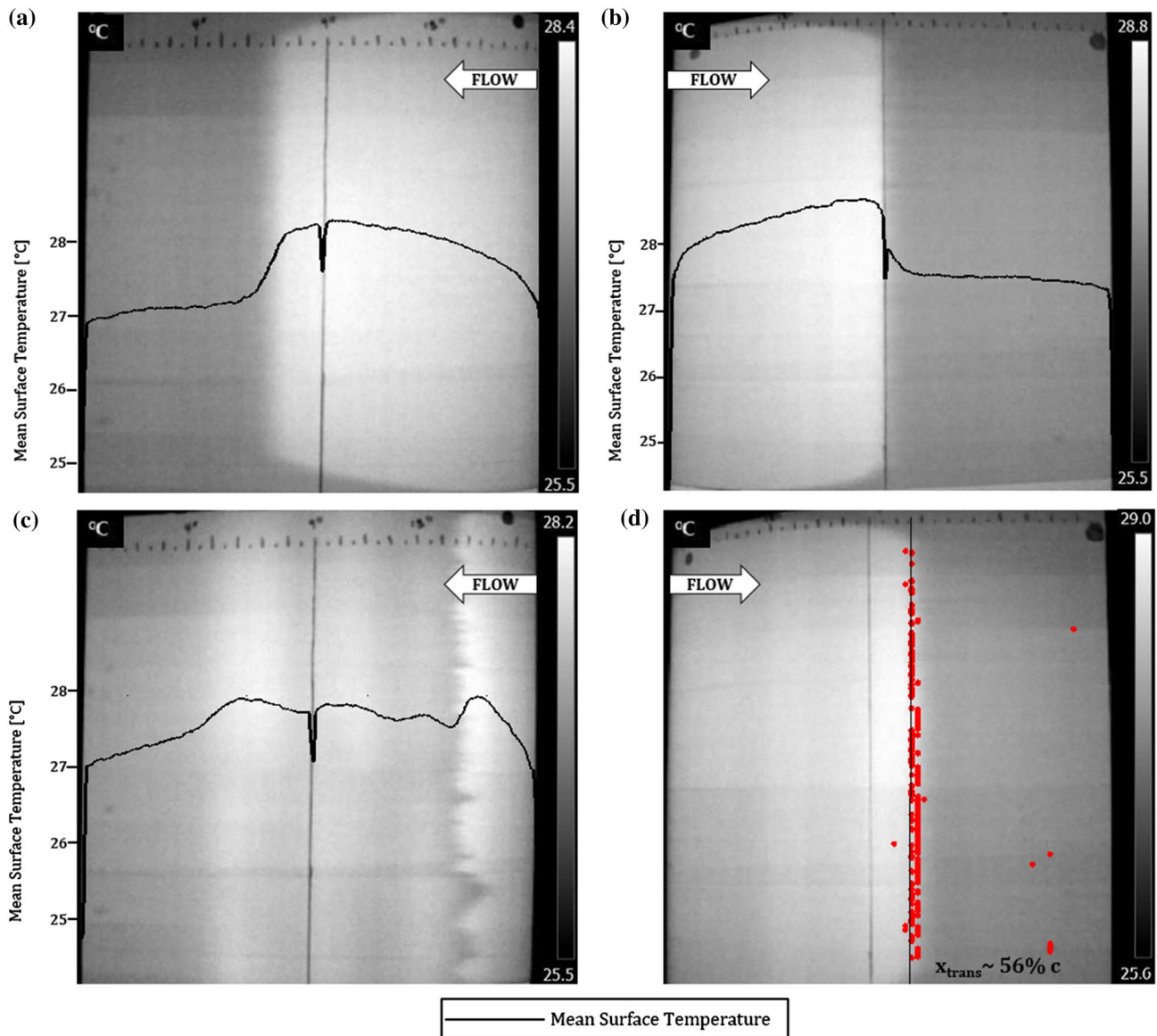


**Fig. 8** Infrared Images of the 0.46-m DU96-W-180 at  $Re = 1.5 \times 10^6$  and **a**  $\alpha_c = 0^\circ$  on pressure side, **b**  $\alpha_c = 0^\circ$  on suction side, **c**  $\alpha_c = -5^\circ$  on pressure side and **d**  $\alpha_c = -7^\circ$  on suction side, with location of highest temperature gradient identified by the image processing algorithm as *dots*

each image and spanwise averaged over the mid 80 % of the insulated area. This drop in temperature is not step-like but occurs progressively over a region of the chord. This finding presumably reflects the fact that transition occurs over a region of flow, rather than at a discrete point.

The temperature gradient indicative of transition is seen to occur as a clean, spanwise uniform, front at most attached-flow angles of attack (example Fig. 8a, b). However, the front develops a jagged pattern for angles of attack approaching and just after stall as well as at some smaller angles (example Fig. 8c). The latter observation, along with the small rise in drag detected in Fig. 7b above angle of attack of  $3^\circ$ , could be interpreted as local

separation, but the corresponding pressure distributions indicate that separation does not occur. Therefore, the nonuniform transition line observed in images like Fig. 8c is most likely due to the increased sensitivity of the thinner boundary layer to surface imperfections as the angle of attack is increased. Local three-dimensional, turbulent flow develops in the vicinity of these surface imperfections forming an irregular transition front. This result shows the sensitivity of the system and its ability to detect subtleties in the transition phenomenon that neither the mean pressure nor stethoscope methods could capture. Qualitatively similar results were observed on both airfoils for all test conditions.

Figure 8d shows a sample processed infrared image at  $\alpha_c = -7^\circ$ , showing the inferred transition location. The algorithm used finds the highest chordwise temperature gradients in the image which coincide with the leading edge, the trailing edge, the line drawn 228.6 mm from the trailing edge, and the transition location. It then uses the first three of these locations to calculate the edge length of the transition location which is then converted to a chordwise location (shown in Fig. 8d). The position estimates produced by this algorithm are predicted to be accurate within  $\pm 5$  mm. This translates to  $\pm 0.6$  % chord at about 30 % chord on the pressure and suction sides of the 0.8-m DU96-W-180 and  $\pm 1.1$  % chord at about 30 % chord on the pressure and suction sides of the 0.46-m DU96-W-180). The local transition location is marked in this figure by a series of dots (one for each vertical pixel in the image), and the final location is taken as the mode of these locations, which is the solid line drawn through the dots.

Similar results were obtained for all angles of attack and flow conditions where transition was detected. Note that all images were clear and obtained rapidly, the response of the system requiring only about 1 s for the flow and image to settle after changing the angle of attack.

### 6.1 Heat transfer analysis

The realism of the temperature changes ascribed to transition was assessed through a heat transfer analysis. The analysis used the electrical analogy for conduction heat transfer (to model heat transfer between heaters and aluminum), boundary layer heat transfer calculations (to estimate the heat transfer in the boundary layer) and the conductive heat transfer equation shown in Eq. 1 (for the heat transfer from the metal model to the surface through the insulator).

$$T_w = \left( T_{Al} - \frac{t_{ins} \dot{Q}}{k_{ins} A_{ins}} \right) \quad (1)$$

In this equation,  $T_w$  is the model surface (wall) temperature,  $T_{Al}$  is the temperature of the aluminum,  $t_{ins}$  is the thickness of the insulator,  $\dot{Q}$  is the rate of heat transfer,  $k_{ins}$  is the thermal conductivity of the insulator and  $A_{ins}$  is the area over which the heat transfer occurs.

The boundary layer heat transfer analysis, used to estimate  $\dot{Q}/A_{ins}$ , is done using online engineering applets, WALZHT (computes incompressible laminar boundary layers with heat transfer using the Thwaites-Walz integral methods) and MOSESHT (computes incompressible turbulent boundary layers using Moses' method extended to include heat transfer). Information about these engineering applets is detailed in Devenport and Schetz 1998. This was done for the suction side of the 0.46-m DU96-W-180

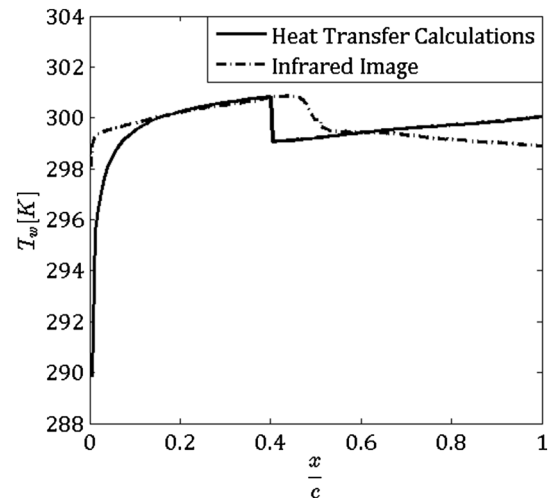


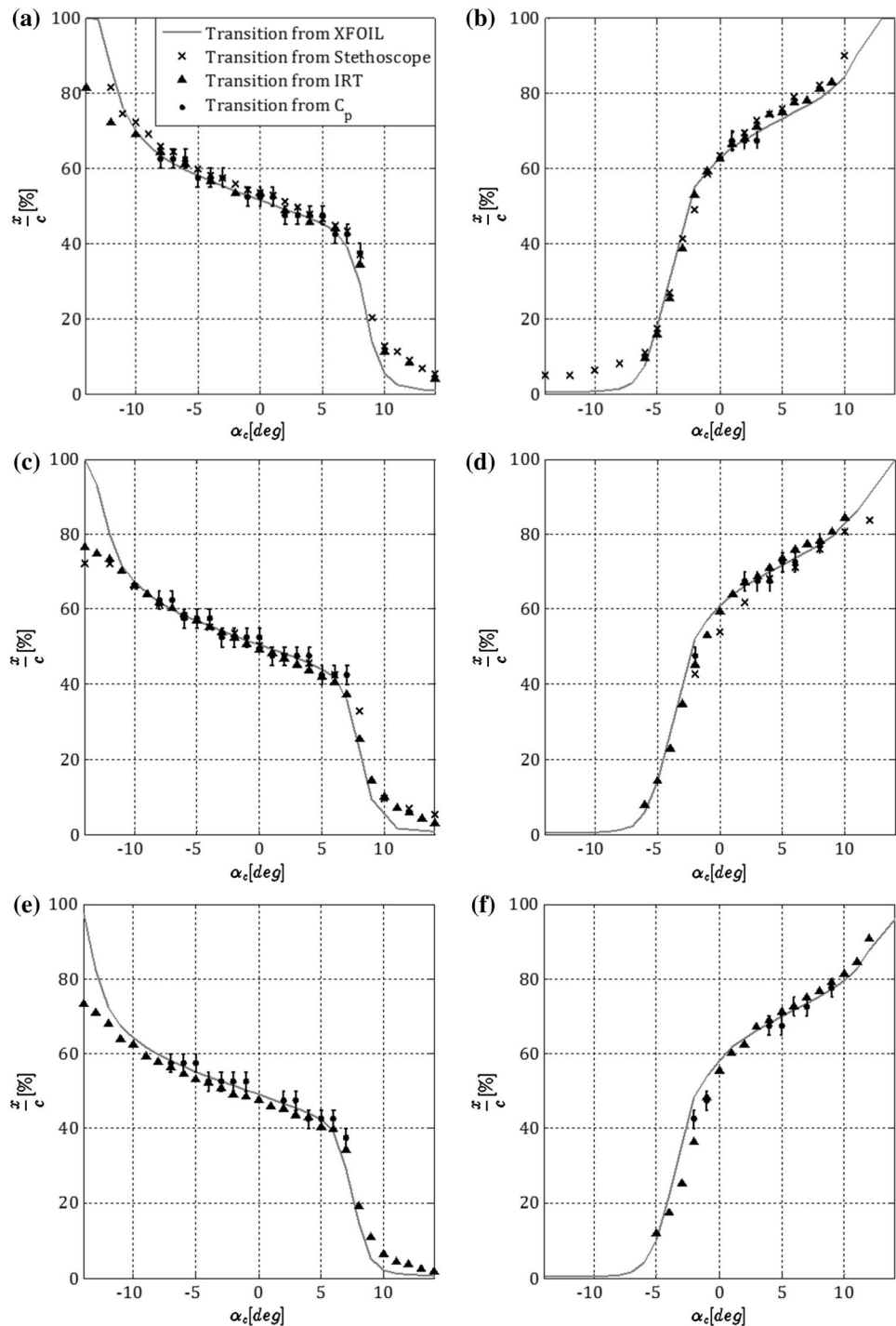
Fig. 9 Comparison of heat transfer calculations with infrared results

model at  $0^\circ$  angle of attack and Reynolds Number of  $2 \times 10^6$  (and all the same experimentally measured flow properties at this condition). The insulator thickness,  $t_{ins}$ , was set as 0.8 mm and the thermal conductivity of the insulator,  $k_{ins}$ , was taken as 0.1 W/(m K). No measurements of the aluminum temperature,  $T_{Al}$ , were made, so this value was fixed at 302.1 K in order to match the wall temperatures with those observed using the IR system at the 30 % chord location. This estimate was typically 9.1 K greater than the flow temperature, roughly consistent with expectations. This means, of course, that the absolute temperatures predicted by the method are guaranteed to match those measured at the 30 % chord location. However, what is of interest here is the magnitude of the temperature change at transition.

The results of this analysis, in terms of model surface temperature at varying chordwise locations, are presented in Fig. 9 for the suction side of the 0.46-m DU96-W-180 model at  $0^\circ$  angle of attack and Reynolds Number of  $2 \times 10^6$ . Normalized chord location is shown on the x-axis, while surface temperature (in Kelvin) is on the y-axis. In this figure, it is seen that the heat transfer model estimates transition occurring about 5 % chord upstream of where it is observed on the infrared image. Both cases show that the temperature close to the leading edge is lower than other points in the laminar region. This has been observed in other similar simulations (Freels 2012). The temperature in the laminar region for both methods reach the same maximum (300.9 K) before dropping off in the turbulent region as transition occurs. The temperature difference estimated by the heat transfer model is 1.7 K, while the temperature difference observed on the infrared images is 1.4 K. Since the model presumes transition at a point, it shows an abrupt temperature drop rather than the more gradual drop



**Fig. 10** Comparison of transition results obtained from four methods for 0.8-m DU96-W-180 **a** suction side at  $Re = 1.5 \times 10^6$ , **b** pressure side at  $Re = 1.5 \times 10^6$ , **c** suction side at  $Re = 2 \times 10^6$ , **d** pressure side at  $Re = 2 \times 10^6$ , **e** suction side at  $Re = 3 \times 10^6$ , **f** pressure side at  $Re = 3 \times 10^6$



observed in the infrared image. Note that the temperatures of measurement and model are within 1 K of each other in the laminar region (ignoring the region close to the leading edge) and within 2 K of each other in the turbulent region.

A similar analysis was done for the pressure side of the 0.46-m DU96-W-180 model at  $0^\circ$  angle of attack and Reynolds Number of  $2 \times 10^6$  which produced results that were consistent with that of the suction side. The temperature

difference estimated by the heat transfer model for the pressure side was 1.4 K, while the temperature difference observed on the infrared images was 1.0 K.

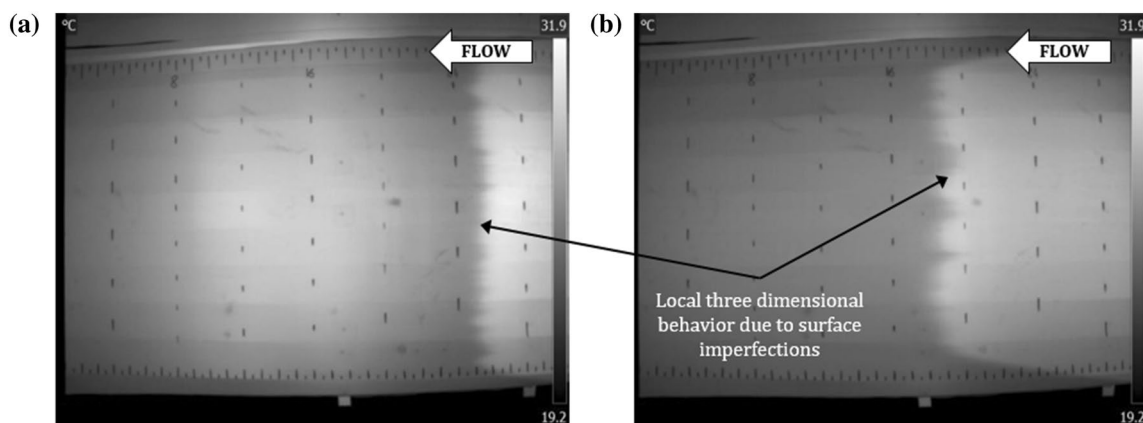
It is important to note that the effect of curvature on signal intensity was considered negligible during this analysis because the change in signal intensity with camera angle relative to the surface was experimentally proven to be small.

## 6.2 Validation

Figure 10 compares results from the IRT, mean pressure analysis, stethoscope measurements and XFOIL calculations for the 0.8-m DU96-W-180 at three Reynolds Numbers. The plots on the left are of the suction side, while the plots on the right are of the pressure side. All results are plotted with corrected angle of attack,  $\alpha_c$ . For all Reynolds numbers and on both sides of the airfoil, the results produced by the infrared thermography system show acceptable agreement with both the mean pressure and stethoscope results for transition. At all angles of attack, the results are consistently within  $\pm 2\%$  chord of each other. The stethoscope measurements and the infrared measurements show the expected curve shape for both the pressure and suction side. The mean pressure results deviate somewhat from the expected curve shape because of the 5% uncertainty. Note that IRT transition results could be obtained for a greater range of angles, even past stall, than the other two experimental methods. The stethoscope measurements are especially dependent on the flow conditions because at high speed or high angle of attack inserting the probe into the flow and keeping it flat against the model was not always possible. This was the case at  $Re = 3 \times 10^6$  in Fig. 10e, f where there are no stethoscope results to report because the speed was too high to insert the probe. Notice also the higher deviations between the stethoscope measurements and the IRT results on the pressure side of the model which is more curved than the suction side, preventing the apparatus from sitting flat against the model. XFOIL appears least able to predict transition past stall where predictions begin to significantly deviate from the infrared thermography transition results, for example, on the pressure side at  $Re = 3 \times 10^6$  and  $\alpha = [-3^\circ: 3^\circ]$  shown in Fig. 10f. The

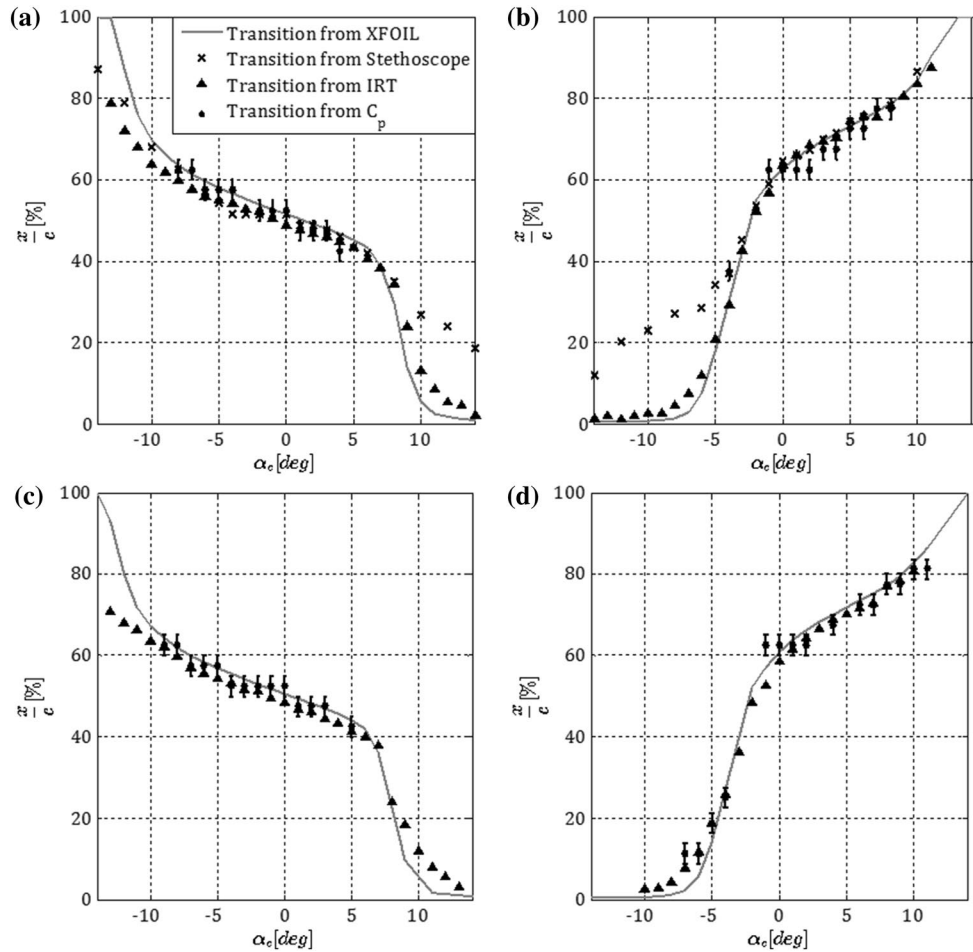
infrared images of the pressure side at two such angles ( $\alpha = -3^\circ, -1^\circ$ ) are presented in Fig. 11. These images show that the transition front is jagged because of local three-dimensional flow (due to local transition over surface imperfections) which explains why the XFOIL prediction, which does not account for 3D effects, are different from the infrared thermography transition results. The IRT system though appears to still be able to detect transition under these circumstances.

Figure 12 presents the comparisons for the pressure and suction side of the 0.46-m DU96-W-180 at two Reynolds Numbers. As was the case with the 0.8-m model, the transition location results from the three experimental methods and XFOIL agree well with each other at most angles of attack. In Fig. 12, it is seen that the stethoscope data deviates from the infrared thermography results by as much as 20% chord at angles higher than  $5^\circ$  on the suction side and at angles less than  $-5^\circ$  on the pressure side. This error in the stethoscope result is attributed to the difficulty of traversing the stethoscope over the curved leading edge of the shorter chord model. Another source of error in the stethoscope measurement comes from inserting the Pitot probe into the flow, which in itself induces transition ahead of the probe and therefore ahead of the natural transition location. This problem is inherent to the stethoscope approach because, unlike the IR technique, it is an intrusive, local detection method. The effect of the probe on the flow is presented in Fig. 13 which shows infrared images before and after inserting the Pitot probe close to the transition location. This effect adds another level of uncertainty to the stethoscope measurements which cannot be precisely quantified because it varies with the angle of attack. However, what is certain is that the transition location detected by the stethoscope will be further upstream than the actual transition.

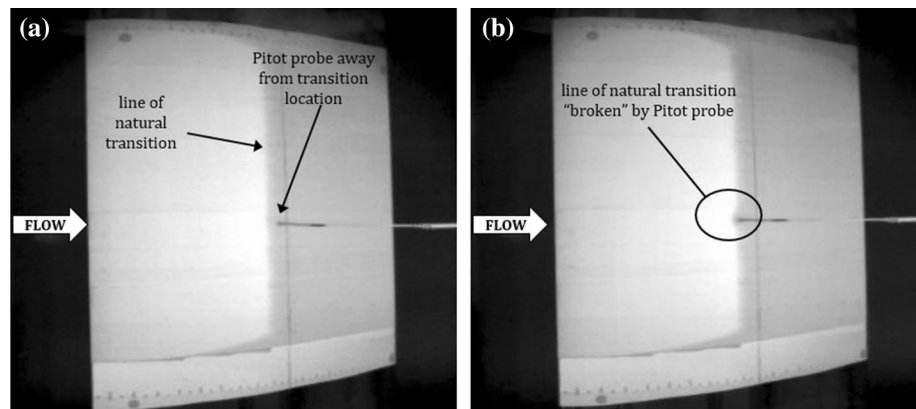


**Fig. 11** Infrared images showing local three-dimensionality of transition for pressure side of the 0.8-m DU96-W-180 at  $Re = 3 \times 10^6$  and **a**  $\alpha_c = -3^\circ$ , **b**  $\alpha_c = -1^\circ$

**Fig. 12** Comparison of transition results obtained from four methods for 0.46-m DU96-W-180 **a** suction side at  $Re = 1.5 \times 10^6$ , **b** pressure side at  $Re = 1.5 \times 10^6$ , **c** suction side at  $Re = 2 \times 10^6$ , **d** pressure side at  $Re = 2 \times 10^6$



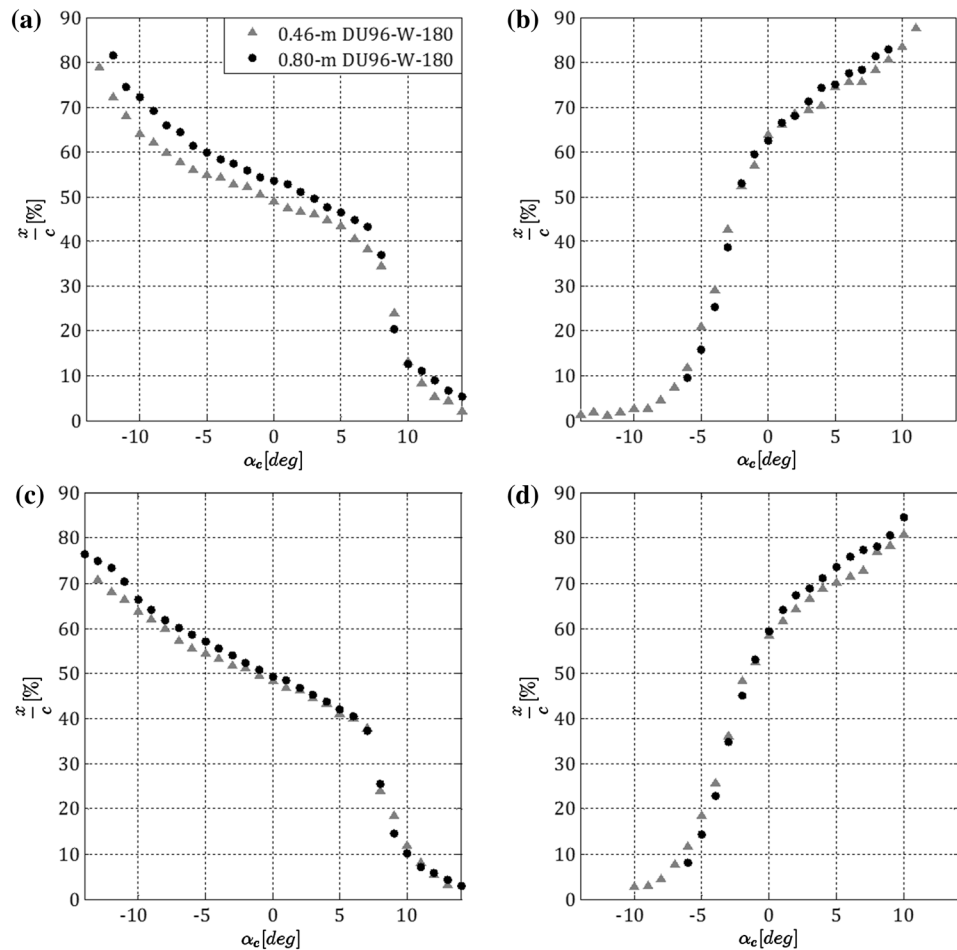
**Fig. 13** Infrared images showing the **a** before and **b** after interference effects of inserting a Pitot tube into the boundary layer of the 0.48-m DU96-W180 (at  $\alpha_c = 8^\circ$ ,  $Re = 2 \times 10^6$ )



As a final validation, the results of the two models, 0.46- and 0.8-m chords, were plotted against each other. Results are presented in Fig. 14. Overall, the data from both models appear to agree well. On average, differences between the results are about 2 % chord but reach a maximum variation of 5 % chord on the suction side at  $Re = 1.5 \times 10^6$ . These variations are most likely due to increases in turbulence

levels associated with increases in flow speed (higher speeds are needed for the shorter chord to be able to reach the same Reynolds Number as the larger chord). Increased turbulence levels will result in earlier transition. Another possible source of discrepancy between the two models is the wall interference which tends to increase the pressure on the side of the model producing positive pressure

**Fig. 14** Effect of chord length of DU96-W-180 on the infrared thermography transition results, investigated on **a** suction side at  $Re = 1.5 \times 10^6$ , **b** pressure side at  $Re = 1.5 \times 10^6$ , **c** suction side at  $Re = 2 \times 10^6$ , **d** pressure side at  $Re = 2 \times 10^6$



(suction side at negative angles and pressure side at positive angles).

### 6.3 Boundary layer flow diagnostics

Occasionally during testing, turbulent wedges distinct from the overall transition line were observed on the infrared images. Since this was observed in real time, the tests were paused and the source of the wedges was investigated as they appeared. In all cases, it was found that some surface imperfection had initiated local transition, thereby producing the wedge. In some cases, the imperfection was due to contaminants in the flow which were transferred to the model surface, while in most cases it was due to small air bubbles forming beneath the ConTact© paper as the temperature was varied. Figure 15 shows a roughly 1-mm tall air bubble which formed on the 0.46-m DU96-W-180 model at  $\alpha = 5^\circ$  and  $Re = 1.5 \times 10^6$  and the wedge that was observed on the IR image.

These observations demonstrate the capability of the infrared thermography system to serve as a flow diagnostic tool during wind tunnel tests.

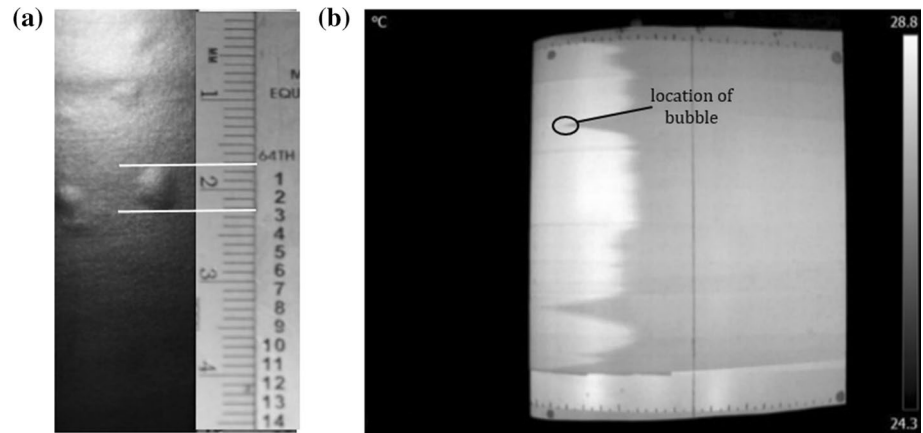
## 7 Conclusions

A boundary layer transition detection system was developed, implemented and validated. This system utilizes infrared thermography to visualize the inherent rise in heat transfer which occurs as laminar flow becomes turbulent, and then extracts the chordwise transition location through image processing techniques. Unlike most other IR systems, the technique is suitable for metal and other models in low-speed flows. In addition, this work details the analysis and validation of the IR system, a topic which has not been widely addressed in literature.

The performance of the system was established through a series of tests on DU96-W-180 airfoils performed at Reynolds numbers from  $1.5 \times 10^6$  to  $3 \times 10^6$  and over a range of angles of attack from  $-15^\circ$  to  $15^\circ$ . Transition locations determined with the system were found to agree, to within combined uncertainty, and with independent measurements made using a stethoscope and the airfoil mean pressure distribution.

The IR system is capable of determining transition location within 5 mm, when observed from a standoff distance

**Fig. 15** **a** 5-mm air bubble formed in ConTact® paper on model surface and **b** infrared image showing the turbulent wedge produced by the air bubble



of 762 mm. In the present work, this corresponded to  $\pm 0.6\%$  chord on the 0.8-m DU96-W-180 and  $\pm 1.1\%$  chord on the 0.46-m DU96-W-180. The system appears to be robust and efficient and capable of continuous measurement over extended wind tunnel runs.

**Acknowledgments** The authors wish to thank General Electric Power and Water for their financial support of this project under the 2013 GE University Strategic Alliance program.

## References

- Allen HJ, Vincenti WG (1947) Wall interference in a two-dimensional flow wind tunnel, with consideration of the effect of compressibility. NACA report, no. 782
- Baek P, Fuglsang P (2009) Experimental detection of transition on wind turbine airfoils. European wind energy conference
- Crawford BK, Duncan GT Jr, West DE, Saric WS (2014) Quantitative boundary-layer transition measurements using IR thermography. AIAA SciTech, 13–17 January 2014, National Harbour, MD
- Dagenhart J, Stack J, Saric W, Mousseux M (1989) Crossflow-vortex instability and transition on a 45 deg swept wing. In: 20th fluid dynamics, plasma dynamics and lasers conference, Buffalo, NY, 12–14 June 1989
- De Luca L, Carlomagno GM, Buresti G (1990) Boundary layer diagnostics by means of an infrared scanning radiometer. *Exp Fluids* 9:121–128
- De Luca L, Guglieri G, Cardone G, Carlomagno GM (1995) Experimental analysis of surface flow on a delta wing by infrared thermography. *AIAA J* 33(8):1510–1512. doi:10.2514/3.12574
- Devenport WJ, Schetz J (1998) Boundary layer codes for students in Java. ASME 1998 fluids engineering division summer meeting, Washington DC, June 21–25
- Ehrmann RS, White EB (2014) Influence of 2D steps and distributed roughness on transition on a NACA 633-418. AIAA SciTech, 13–17 January 2014, National Harbor, MD
- Freels JR (2012) An examination of configurations for using infrared to measure boundary layer transition. M.S. Thesis, Aerospace Engineering, Texas A&M University
- Gaidos EJ (1990) Remote infrared thermography for boundary layer measurements. M.S. Thesis, Aeronautics and Astronautics, MIT
- Gompertz K, Bons JP, Gregory JW (2012) Passive trip evaluation using infrared thermography. American Institute of Aeronautics and Astronautics, Inc.
- Joseph LA (2014) Transition detection for low speed wind tunnel testing using infrared thermography. M.S. thesis, Aerospace Engineering, Virginia Tech
- Joseph LA, Aurelien B, Devenport WJ (2014) Transition detection for low speed wind tunnel testing using infrared thermography. 30th AIAA aerodynamic measurement technology and ground testing conference. Atlanta, Georgia
- Le Sant Y, Marchand M, Millan P, Fontaine J (2002) An overview of infrared thermography techniques used in large wind tunnels. *Aerosp Sci Technol* 6:355–366
- Maughmer MD, Coder JG (2010) Comparisons of theoretical methods for predicting airfoil aerodynamic characteristics. Airfoils, Incorporated, Port Matilda
- Mueller TJ (2001) Fixed and flapping wing aerodynamics for micro air vehicle applications. American Institute of Aeronautics and Astronautics
- Patorski J, Bauer GS, Dementjev S (2000) Two-dimensional and dynamic (2DD) method of visualization of the flow characteristics in a convection boundary layer using infrared thermography. In: Dinwiddie RB, LeMieux DH (eds) *Thermosense XXII*, vol 4020
- Popov AV, Botez RM, Labib M (2008) Transition point detection from the surface pressure distribution for controller design. *J Aircr* 45(1):23–28
- Quast A (1987) Detection of transition by infrared image technique. 12th International congress on instrumentation in aerospace simulation facilities, Williamsburg, VA, June 22, 25
- Radzetsky R Jr, Reibert M, Saric W (1994) Development of a stationary crossflow vortices on a swept wing. In: 25th AIAA fluid dynamics conference, Colorado Springs, CO, 20–23 June 1994
- Ricci R, Sergio Montelpare S (2009) Analysis of boundary layer separation phenomena by infrared thermography—use of acoustic and/or mechanical devices to avoid or reduce the laminar separation bubble effects. *Quant InfraRed Thermogr J* 6(1):101–125
- Schmitt RL, Chanetz BP (1985) Experimental investigation of three dimensional separation on an ellipsoid cylinder body at incidence. AIAA 18th fluid dynamics and plasma dynamics and lasers conference, Cincinnati OH, July 16–18. AIAA-85-1686
- Tropea C et al (2007) Springer handbook of experimental fluid mechanics. Springer, New York, p. 896
- Yokokawa Y (2005) Transition measurement on metallic aircraft model in typical low speed wind tunnel. *Trans Jpn Soc Aeronaut Space Sci* 48(161):175–176
- Zuccher S, Saric WS (2008) Infrared thermography investigations in transitional supersonic boundary layers. *Exp Fluids* 44:145–157